Materials Science & Engineering A 757 (2019) 160–171

Contents lists available at ScienceDirect

Materials Science & Engineering A

journal homepage: www.elsevier.com/locate/msea

The microstructure and mechanical properties of novel Al-Cr-Fe-Mn-Ni high-entropy alloys with trimodal distributions of coherent B2 precipitates

L.J. Zhang[a], K. Guo[a], H. Tang[a,b], M.D. Zhang[a], J.T. Fan[a], P. Cui[a], Y.M. Ma[a], P.F. Yu[a,*], G. Li[a,**]

[a] State Key Laboratory of Metastable Materials Science and Technology, Yanshan University, Qinhuangdao, 066004, China
[b] Center for High Pressure Science and Technology Advanced Research, Beijing, 100094, China

ARTICLE INFO

Keywords:
High-entropy alloy
Coherent precipitates
Multimodal distributions
Microstructural evolution
Strengthening mechanisms

ABSTRACT

A series of novel Co-free $Al_xCrFeMnNi$ (x = 0.5–0.8) high-entropy alloys (HEAs) with trimodal distributions of coherent B2 precipitates was fabricated. A fundamental investigation on the microstructural evolution and mechanical properties of these trimodal alloys was conducted. Structural characterization shows that these HEAs possess complex microstructures consisting of a disordered body-centered-cubic (BCC) matrix and trimodal-size distributions of the ordered coherent B2 precipitates, (1) the primary B2 (p-B2) precipitates with a mean length of ~2 μm located in the interdendritic region, (2) the secondary B2 (s-B2) precipitates with a mean diameter of ~450 nm, and (3) the tertiary B2 (t-B2) precipitates with a mean diameter of ~20 nm located in the dendritic region. The trimodal HEAs exhibit a good combination of high compressive yield strengths of 1091–1200 MPa and the large plasticity (> 45%). The increments of the yield strengths caused by different strengthening mechanisms have been quantitatively and respectively estimated and compared with the experimental measurements. The study of the present trimodal BCC-B2 HEAs can provide a useful guidance for the future development of multimodal BCC-based HEAs with excellent properties.

1. Introduction

The development of the new alloy-design concept plays a crucial role in the exploration of novel metallic materials with excellent properties. Recently, many researchers have focused their attention on the high-entropy alloys (HEAs) and multi-component alloys, which were first independently and respectively reported by Yeh et al. [1] and Cantor et al. [2]. Different from the traditional strategy, HEAs are not based on only one or two principal elements but generally contain at least five principal elements in equimolar or near-equimolar proportions [3,4]. The equiatomic or near-equiatomic HEA design aims at the maximization of the configurational entropy with the purpose of stabilizing the solid-solution phase [3]. HEAs are often treated as the multi-component solid-solution alloys with simple crystal structures, e.g., the face-center-cubic (FCC) phase, body-center-cubic (BCC) phase, hexagonal-close-packed (HCP) phase, or their mixtures [1,5–7]. A unique combination of the topological order and chemical disorder in HEAs can discriminate them from bulk metallic glasses (BMGs) and conventional crystals in the field of materials science. HEAs display a variety of technologically-appealing properties, such as the superb specific strength [4,8], good fatigue behavior [9–12], oxidation and corrosion resistance [13–17], radiation tolerance [18,19], and superconductivity [20,21], etc. Due to these attractive properties, HEAs are promising candidates for technological applications in many fields, such as elevated-temperature applications [22], nuclear energy industry [23], space exploration, and storage of cryogens [24]. Recently, numerous studies have focused on the mechanical properties and deformation mechanisms of the FCC-based HEAs. For example, the thermally-activated process of deformation in the CoCrFeMnNi HEA has been investigated at room temperature and liquid nitrogen temperature [25]. The FCC HEAs with good ductility are often treated as the excellent base for further strengthening through precipitation strengthening by adding elements and thermal-mechanical processing [26–28], grain boundary and dislocation strengthening by severe plastic deformation [29,30], etc. However, few dedicated studies about the mechanical-performance optimization and the deformation process of the BCC-based HEAs are available in the literature.

Among HEAs, the BCC-based HEAs often show poor ductility despite their high strength [31–33]. For instance, the typical equiatomic AlCoCrFeNi HEA has a high compression yield strength of 1308 MPa and low plasticity of 5.6%, due to a weave-like microstructure induced by the spinodal decomposition of BCC and B2 phases [31]. The poor

* Corresponding author.
** Corresponding author.
E-mail addresses: ypf@ysu.edu.cn (P.F. Yu), gongli@ysu.edu.cn (G. Li).

https://doi.org/10.1016/j.msea.2019.04.104
Received 25 January 2019; Received in revised form 23 April 2019; Accepted 27 April 2019
Available online 28 April 2019
0921-5093/

ductility limits their use for structural applications. In order to improve the ductility of these alloys, the density of coherent boundaries between the BCC and B2 phases can be increased and a multimodal structure instead of the weave-like microstructure can be designed. On the one hand, Lu et al. [34,35] have pointed out that some coherent boundaries can not only block dislocation motion, but also absorb and accommodate dislocations. Improving the stability of coherent boundaries can effectively increase the strength and ductility. Jiang et al. [36] created a class of ultrastrong steels, with high-density coherent B2 nanoprecipitates, having a tensile strength of up to 2.2 GPa and good ductility of about 8.2%. The low coherent strain can effectively prevent the crack initiation at the precipitate-matrix interfaces. Fu et al. [37]. fabricated a bulk $Fe_{25}Co_{25}Ni_{25}Al_{10}Ti_{15}$ HEA containing hierarchical intragranular nanoprecipitates with a high tensile yield strength of ~1.86 GPa and failure strain of ~5.2%. The $Fe_{36}Mn_{21}Cr_{18}Ni_{15}Al_{10}$ HEA, with the high density cuboidal B2 ordered particles embedded in a BCC matrix, had a yield strength of 990 MPa and a high compression ductility (> 50%) in compression [38,39]. On the other hand, the multimodal structure strategy is effective in optimizing strength and plasticity. The multimodal distributions can relax the stress concentration, due to the crystalline phases with different length scales will have various abilities to accommodate the local strain upon deformation. Yang et al. [40] synthesized a novel $(Ti_{63.5}Fe_{26.5}Co_{10})_{82}Nb_{12.2}Al_{5.8}$ bimodal titanium alloy with B2 phase and β-Ti phases, which exhibits the ultrahigh compressive yield strength of 2050 MPa and high compressive plasticity of 19.7%. In the present work, the trimodal $Al_xCrFeMnNi$ (x = 0.5–0.8) HEAs were fabricated to take advantage of the benefits associated with coherent boundaries and multimodal structures.

The composition design of the current HEAs based on the cluster-plus-glue-atom model, which was proposed based on the chemical short-range orders (CSROs) between solute atoms and solvent atoms [41,42]. In this model, an alloy structure can be dissociated into a cluster part and a glue atom part, where the cluster part is the nearest-neighbor polyhedron centered by a solute atom having strong interactions with the base solvent atoms, and the glue part is the other solute atoms with weak interactions situating at the interstitial sites between the clusters. Thus, the structure can be expressed by a cluster formula of $[cluster](glue\ atom)_n$, where n is the glue atom number to match one cluster. The nearest-neighbor cluster for the FCC solid solution is a CN12 (CN: coordination number) cuboctahedral cluster. A rhombi-dodecahedron with CN14 is the cluster part for the BCC solid solution. This cluster-formula approach has been applied to HEAs, and the cluster model has been validated by neutron experiments [43].

In the Al-Cr-Fe-Mn-Ni system, the mixing enthalpies (ΔH_{AB}^{mix}) between Al and the four transition metals (TMs) show more negative values than those between TMs (see Ref. [44] or Table 1), which indicates that Al has strong interactions with these TMs, and TMs exhibit only weak mutual interactions. Consequently, Al and TMs are regarded as the solute atom and solvent atoms, respectively. The $Al_xCrFeMnNi$ series can be simply expressed by Al_xM_4, where $M = Cr_1Fe_1Mn_1Ni_1$ is an equimolar mixing of these TMs. From the cluster formulas of the $[Al\text{-}M_{12}](M_2Al_1)$ in the FCC structure and the $[Al\text{-}M_{14}]Al_1$ in the BCC structure, one can obtain the alloy composition of Al_2M_{14} [or $Al_{12.5}M_{87.5}$, atomic percent (at. %)], which is very close to the upper limit of the single-phase FCC region (i.e., $Al_{0.5}M_4$ or $Al_{11.1}M_{88.9}$) from experiments [45]. Further increasing the Al content can produce a large lattice distortion. A structural transition from FCC to BCC/B2 phases will happen to relax the lattice-distortion energy [46]. At the same time, the morphology of the BCC/B2 phases will also change from the plate structure to nanophase precipitate and spinodally-decomposed structure, depending on the observations in other Al-TMs HEA systems, e.g., $Al_xCoCrFeNi$, $Al_xCoCrCuFeNi$, and $Al_xCoCrFeMnNi$ [45–47].

Therefore, in our work, a series of new Al-Cr-Fe-Mn-Ni HEAs are designed and synthesized, based on the composition formula of Al_xM_4 ($x \geq 0.5$). The specific chemical compositions (at. %) of these alloys are summarized in Table 2. Furthermore, the expensive cobalt was removed to reduce the alloy cost and increase the potential applicability of the present alloy system. Finally, the novel $Al_xCrFeMnNi$ (x = 0.5–0.8) HEAs were prepared with a BCC matrix and trimodal distributions of coherent B2 precipitates. A systematic investigation of the structural evolution, mechanical properties, and strengthening mechanisms of the trimodal HEAs was conducted.

Table 1
Melting point (T_i), shear modulus (μ_i), atomic radius (r_i), and valence electron concentration (VEC) of the ith element, and the mixing enthalpy of different atom pairs, ΔH_{AB}^{mix}(kJ/mol), in the $Al_xCrFeMnNi$ HEAs calculated by the Miedema's approach [44].

Element (T_i, μ_i, r_i, VEC_i)	Al	Cr	Fe	Mn	Ni
Al (660.3 °C, 26 GPa, 143 pm, 3)	—	−10	−11	−19	−22
Cr (1907 °C, 115.1 GPa, 128 pm, 6)	—	—	−1	2	−7
Fe (1538 °C, 81.4 GPa, 126 pm, 8)	—	—	—	0	−2
Mn (1246 °C, 39 GPa, 127 pm, 7)	—	—	—	—	−8
Ni (1455 °C, 80 GPa, 124 pm, 10)	—	—	—	—	—

2. Experimental procedure

The alloy ingots of $Al_xCrFeMnNi$ (x = 0.5, 0.6, 0.7, and 0.8) HEAs (denoted as A5, A6, A7, and A8, respectively) were synthesized by arc-melting a mixture of pure metals [purity > 99.9 wt percent (wt. %)] in a vacuum arc melting furnace with a water-cooled Cu crucible under a Ti-gettered high-purity argon atmosphere. The ingot with a total weight of about 50 g was remelted at least six times to guarantee the chemical homogeneity.

The phase identifications, crystal structures, and microstructures of all the specimens were characterized by the X-ray diffraction (XRD), scanning electron microscopy (SEM), and transmission electron microscopy (TEM). A D/MAX-2500/PC diffractometer with the Cu Ka radiation (λ = 1.54 Å) was used for the XRD analysis, with a scanning rate of 4°/min from 20° to 100°. The SEM measurements were performed, using a Hitachi S-4800 microscope. The specimens for the SEM observation were prepared by grinding with the silicon-carbide paper to grade 5000, followed by polishing, using the one-micron diamond paste. Then, the polished surfaces were etched with the aqua-regia solution (a mixture formed by freshly-mixing the hydrochloric acid and concentrated nitric acid usually in a volume ratio of 3:1). The TEM observations were performed, using a FEI Talos F200X apparatus equipped with an energy-dispersive X-ray spectrometer (EDS) at an accelerating voltage of 200 kV. The TEM samples were mechanically ground to a thickness of less than 30 μm, and then further thinning was made through ion milling, employing a Precision Ion Polisher (Gatan 695.B). Statistical analyses of the volume fraction, average grain size, and shape factor of the B2 precipitates were performed with at least three SEM or TEM morphology images, using the Image-Pro Plus software [48].

Values of the Vickers hardness of the current HEAs were measured, employing a HVS-1000 hardness tester under a load of 500 g for 15 s. The nanoindentation experiments were conducted, using a Hysitron Triboindenter (TI-900) equipped with a Berkovich diamond tip, with a maximum load of 7 mN under the constant loading rate of 1 mN s^{-1}. The average hardness was taken from at least 10 measurements for each alloy sample. Cylindrical specimens for compression with the aspect ratio of 2:1 (ϕ 3 × 6 mm) were prepared, according to ASTM (American Society for Testing and Materials) standards [49]. Room-temperature compression tests were conducted on an INSTRON-5982 machine under a strain rate of 5×10^{-4} s^{-1}. In order to obtain a real compressive strain, the machine stiffness must be taken into account. Based on the previous method [48], the machine stiffness was measured by compressing a 310S stainless steel sample with a known Young's modulus (205 GPa) in our experiments. Two graphite spacers were inserted between the test specimens and the compression platform to minimize the

Table 2
Data summary for $Al_xCrFeMnNi$ (x = 0.5, 0.6, 0.7, and 0.8) HEAs, including the chemical compositions, mixing entropy (ΔS_{mix}), mixing enthalpy (ΔH_{mix}), atomic-size mismatch (δ), regular solution-interaction parameter (Ω), valence electron concentration (*VEC*), and phase constitution.

No.	M	Chemical compositions (at. %)	ΔS_{mix}	ΔH_{mix}	δ	Ω	*VEC*	Phase
			(J/mol/K)	(kJ/mol)	(%)			constitution
1	$Al_{0.5}CrFeMnNi$ (A5)	$Al_{11.11}Cr_{22.22}Fe_{22.22}Mn_{22.22}Ni_{22.22}$	13.15	−9.28	4.25	2.42	7.22	BCC matrix + B2 phases
2	$Al_{0.6}CrFeMnNi$ (A6)	$Al_{13.04}Cr_{21.74}Fe_{21.74}Mn_{21.74}Ni_{21.74}$	13.24	−10.06	4.52	2.23	7.13	BCC matrix + B2 phases
3	$Al_{0.7}CrFeMnNi$ (A7)	$Al_{14.89}Cr_{21.28}Fe_{21.28}Mn_{21.28}Ni_{21.28}$	13.31	−10.76	4.75	2.08	7.04	BCC matrix + B2 phases
4	$Al_{0.8}CrFeMnNi$ (A8)	$Al_{16.67}Cr_{20.83}Fe_{20.83}Mn_{20.83}Ni_{20.83}$	13.35	−11.39	4.95	1.95	6.96	BCC matrix + B2 phases

errors resulting from the friction problem of both ends. To ensure the reliability and accuracy, at least 4 measurements were carried out for each alloy sample.

3. Results and discussion

3.1. Microstructural characteristics

The XRD patterns of the present A5, A6, A7, and A8 HEAs are shown in Fig. 1. The results indicate the presence of a BCC phase and an ordered B2 phase (based on superlattice reflections) in these HEAs. The microstructures of the four HEAs are investigated by the SEM images presented in Fig. 2. Low-magnification SEM images [see Fig. 2(a), (d), (g), and (j)] show that all of the four alloys have dendritic (DR) and interdendritic (ID) structures. The ID regions contain many rod-shaped precipitates with a length of about 2 μm for each alloy, as presented in Fig. 2(b), (e), (h), and (k). While within the DR regions, a large number of near-spherical precipitates with the size of about 400 nm are embedded in the matrix. The higher-magnification images of the DR regions [see Fig. 2(c), (f), (i), and (l)] indicate that a large amount of small precipitates with the size of about 20 nm also dispersedly distribute in the matrix. The distribution and morphology of the precipitates are similar among the four alloys. However, the volume fractions of the ID and DR regions show a great change by adjusting the Al content in the present alloy system, as exhibited in Fig. 3. For instance, the volume fraction of the ID region is estimated to be only 18.9% in the A5 alloy. In comparison, increasing the Al content can lead to the value significantly increasing to about 46.6% in the A8 alloy.

The EDS elemental-mapping analysis performed on the A8 alloy is presented in Fig. 4. It is clear that the rod-shaped (ID region) and near-spherical (DR region) precipitates are enriched in Al and Ni. The matrix phase is enriched in Cr and Fe. The Mn element is nearly uniformly distributed in the precipitate phase and the matrix. Depending on previous reports in other Al-TMs HEA systems [45–47,50], the ordered B2 phase enriched in Al and Ni is favorable to be formed due to the negative mixing enthalpy of - 22 kJ/mol (see Table 1), and the disordered BCC phase is enriched in Cr and Fe. Accordingly, for the current HEA system, it is possible to suggest that the Al-Ni-rich precipitates are the ordered B2 phase, and the Cr-Fe-rich matrix is the disordered BCC phase. Here, we denote the rod-shaped precipitates, near-spherical precipitates, and small spherical precipitates as the primary B2 (p-B2) phase, secondary B2 (s-B2) phase, and tertiary B2 (t-B2) phase, respectively.

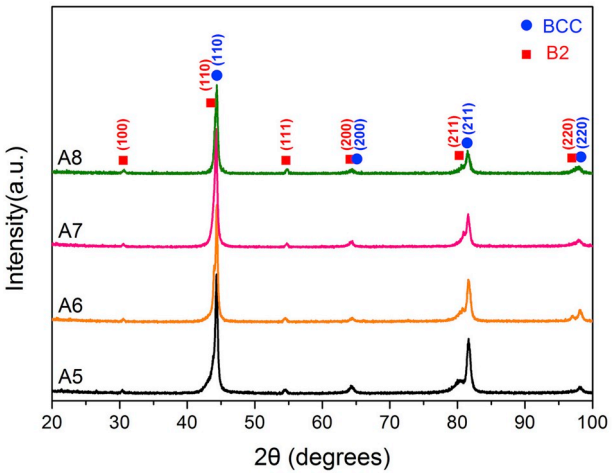

Fig. 1. XRD patterns of the as-cast A5, A6, A7, and A8 HEAs.

In order to further reveal the phase structures of these HEAs in details, the TEM observations were performed. Due to the similar microstructures of the present four trimodal HEAs, we just display the TEM results of the A5 alloy as a representative, as shown in Figs. 5 and 6. In the A5 alloy, the bright-field image of the DR region [Fig. 5(a)] and the high-magnification image [Fig. 5(b)] indicate that the near-spherical s-B2 precipitates (about 300–500 nm in diameter) and small spherical t-B2 precipitates (about 10–50 nm in diameter) are dispersed in the matrix. The crystal structure of the s-B2 precipitates can be identified as the ordered BCC phase by the unique $(\bar{1}00$ and $0\bar{1}0)_{B2}$ superlattice reflections in the selected-area electron diffraction (SAED) patterns, as exhibited in Fig. 5(c). The coherent interface between the s-B2 phase and BCC matrix was examined using HRTEM observation, and the result was shown in Fig. 5(f). The corresponding fast Fourier transform (FFT) images of different area are also presented, indicating the disordered BCC matrix and the ordered s-B2 phase with the {100} superlattice reflections. The FFT image at the interface and the SAED patterns along the [001] zone axis [see Fig. 5(d) and (e)] indicated that the s-B2 and t-B2 phases are actually coherent with the BCC matrix. The rod-shaped p-B2 precipitates (about 2 μm in length) in the ID region are embedded in the matrix, as presented in Fig. 6(a). The TEM results show a good agreement with the SEM observations (Fig. 2). The HRTEM image and the corresponding FFT images are presented in Fig. 6(b). The superlattice diffractions in the FFT pattern of the precipitate indicate that the p-B2 precipitate was an ordered BCC phase. The results also clearly reveal the interfacial coherence between the p-B2 phase and BCC matrix. The similar morphology for the three ordered B2 phases embedded coherently in the disordered BCC matrix has also been observed in the other three HEAs.

To identify the chemical compositions of these B2 precipitates and BCC matrix in the present HEAs, we performed the TEM-EDS point analysis, and the final results are summarized in Table 3. One can note the higher concentrations of Al and Ni in these B2 phases and Cr and Fe in the BCC matrix, which are consistent with the results of EDS maps (Fig. 4).

In summary, the SEM and TEM observations indicate that the present four HEAs possess microstructures consisting of a BCC matrix and the trimodal distributions of coherent B2 precipitates with three orders of magnitudes in the size distributions [i.e., (1) 10^0 μm for the p-B2

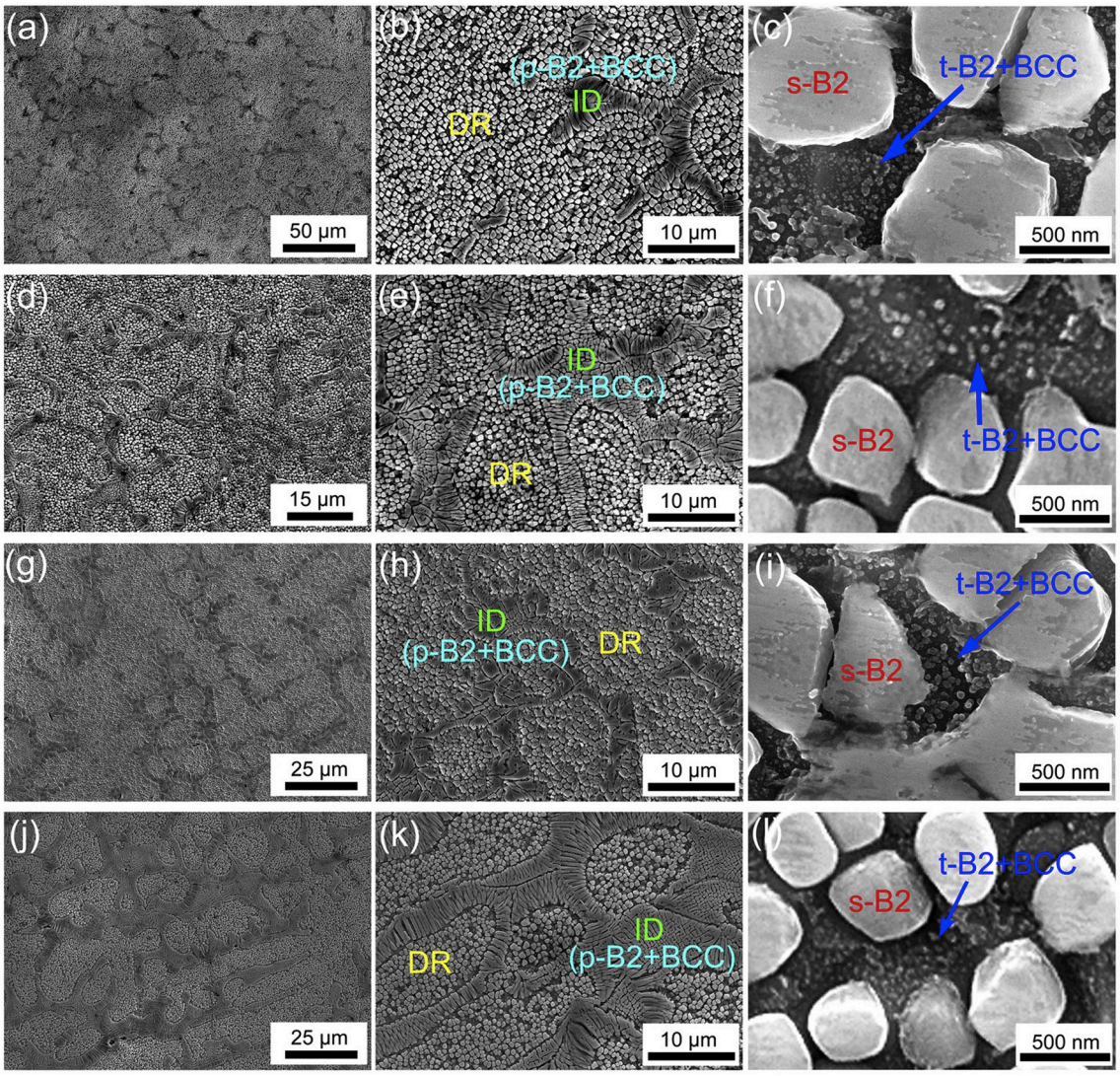

Fig. 2. SEM microstructures of the as-cast A5 (a–c), A6 (d–f), A7 (g–i), and A8 (j–l) HEAs.

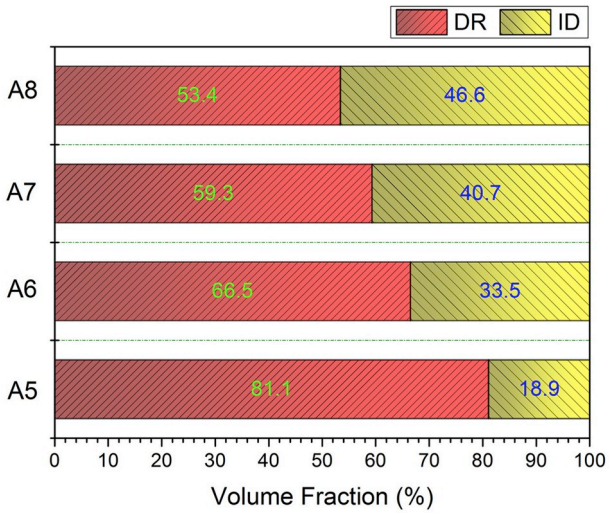

Fig. 3. The volume fractions of DR and ID regions in A5, A6, A7, and A8 HEAs.

precipitates, (2) 10^{-1} μm for the s-B2 precipitates, and (3) 10^{-2} μm for the t-B2 precipitates], which is similar to the multimodal γ' distributions produced in nickel-base superalloys [51,52]. By adjusting the concentration of the Al element, the phase constitutions (see Fig. 1 or Table 2) and the trimodal distribution of coherent B2 precipitates have not changed. The B2 precipitate geometrical parameters, including the average size and volume fraction, show different values in A5, A6, A7, and A8 HEAs. A detailed analysis about the effect of the Al concentration on the structural evolution will be discussed in the next section.

3.2. Effect of the Al concentration on the structural evolution

The Al element, as a strong BCC stabilizer, has a great influence on the crystal structures and microstructures of the conventional alloys and HEAs [45–47,53,54]. For instance, the addition of the large Al element into the FCC-CoCrFeNi(Mn) alloy can not only promote the formation of the BCC phase, but also change the microstructure from the large grains to dendritic structure and spinodally-decomposed structure [45,46]. In the present work, a detailed analysis of the Al concentration on the phase-structure formation and microstructural evolution of the designed trimodal HEAs will be performed.

Recently, researchers have proposed a couple of criteria to predict the phase formation in HEAs. From a thermodynamic point of view, Yang et al. [55] and Zhang et al. [56] have suggested two effective criteria, Ω-δ and ΔH_{mix}-δ, for achieving solid-solution phases in HEAs, where $\Omega = T_m \Delta S_{mix} / |\Delta H_{mix}|$ is the regular solution-interaction

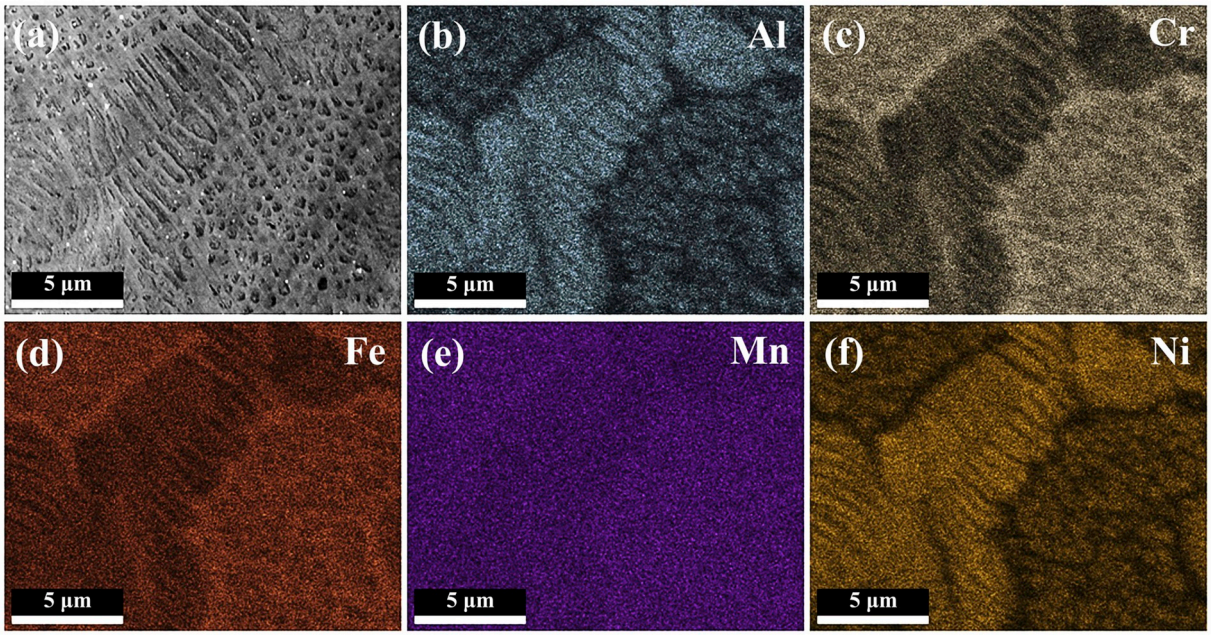

Fig. 4. SEM images and EDS maps of the alloy elements of Al, Cr, Fe, Mn, and Ni for the A8 HEA.

parameter, $T_m = \sum_{i=1}^{n} c_i (T_m)_i$, $(T_m)_i$ is the melting point of the ith constituent element (see Table 1), $\Delta S_{mix} = -R \sum_{i=1}^{n} (c_i \ln c_i)$ is the mixing entropy of an n-component HEA, R is the gas constant; $\Delta H_{mix} = \sum_{i=1, i \neq j}^{n} 4 \Delta H_{AB}^{mix} c_i c_j$ is the mixing enthalpy, ΔH_{AB}^{mix} is the enthalpy of mixing the ith and jth components, based on the Miedema's approach [44], c_i and c_j are the atomic percentages of the ith and jth components; and $\delta = \sqrt{\sum_{i=1}^{n} c_i \left(1 - \frac{r_i}{\bar{r}}\right)^2}$ is the atomic-size difference of the HEA, $\bar{r} = \sum_{i=1}^{n} c_i r_i$ is the average atomic radius, and r_i is the atomic radius of the ith component (see Table 1). For the current trimodal HEAs, the calculated values of these physical parameters are listed in Table 2. According to the criteria of Ω-δ and ΔH_{mix}-δ, stable solid-

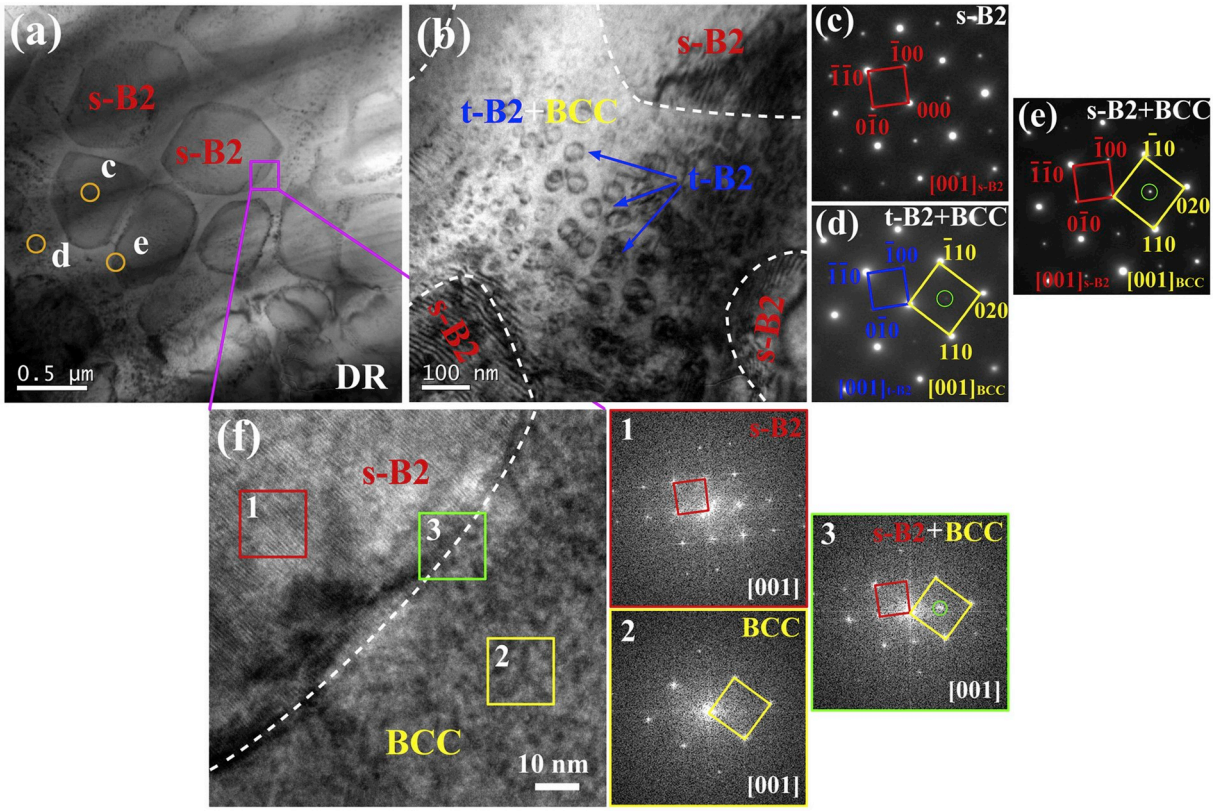

Fig. 5. TEM observations of the DR region in the A5 alloy. The bright-field image of the DR region (a) and the high-magnification image (b) show that the s-B2 and t-B2 precipitates are embedded in the BCC matrix; and the corresponding SAED patterns of the s-B2, t-B2, and BCC phases are presented in (c)–(e) along the [001] zone axis. (f) HRTEM image of the interface indicated by the white line between the s-B2 and BCC matrix in the DR region, the corresponding FFT patterns are also presented.

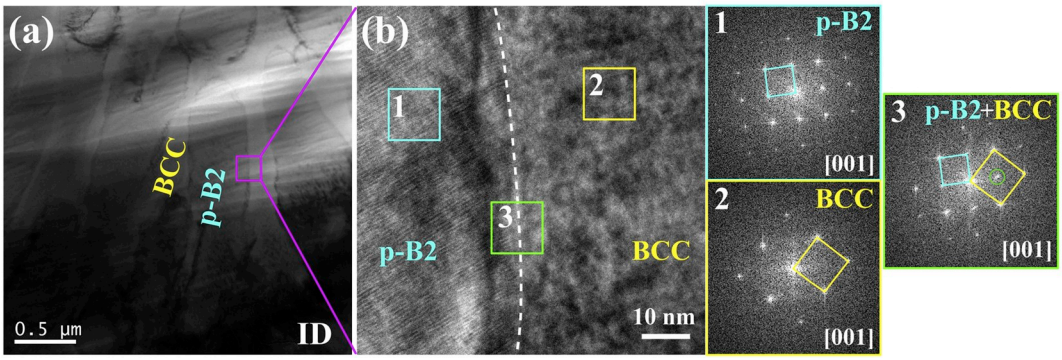

Fig. 6. TEM observations of the ID region in the A5 alloy. The bright-field image of the ID region (a) show that the p-B2 precipitates are embedded in the BCC matrix. (b) HRTEM image of the interface indicated by the white line between the p-B2 and BCC matrix in the DR region, the corresponding FFT patterns are also presented.

solution phases are formed in the region of $\Omega \geq 1.1$ and $\delta \leq 6.6\%$, and $-15\,\mathrm{kJ/mol} < \Delta H_{mix} < 5\,\mathrm{kJ/mol}$ and $\delta < 5\%$ [55,56], using the available data from various HEA systems. As seen from Table 2, these trimodal HEAs should form solid-solution phases. However, these alloys form both disordered BCC phase and ordered B2 phase, suggesting that the two criteria cannot be used to predict these alloys with BCC/B2 phases. Moreover, another parameter, the valence electron concentration (*VEC*), has been proposed to predict the stability of FCC and BCC phases in HEAs [57]. *VEC* for the multi-component HEAs is calculated by $VEC = \sum_{i=1}^{n} c_i (VEC)_i$, where $(VEC)_i$ is the *VEC* value of the *i*th component element (see Table 1). The BCC phase is stable if $VEC \leq 6.87$, while the FCC phase is stable if $VEC \geq 8$. A mixture dual-phase microstructure containing both BCC and FCC phases is favored when $6.87 < VEC < 8$. However, these present trimodal HEAs with $VEC < 7.3$ (see Table 2) exhibit a dual-phase structure with BCC and B2 phases, which is similar to the range ($VEC < 7.35$) of Al-Ni-Co-Fe-Cr BCC/B2 HEAs [48]. Therefore, we need more exquisite criteria to describe the separation of BCC and B2 phases in HEAs.

Both the SEM and TEM observations have suggested that the addition of the Al element could change the size and morphology of the ordered B2 precipitates in the present trimodal HEAs. Histograms of the particle-size distributions of these B2 precipitates were shown in Figs. 7 and 8. Apparently, the three B2 precipitates in the designed HEAs possess the typical trimodal distribution: (1) p-B2 precipitates with a diameter distribution range of 200–1400 nm [Fig. 7(a)] and a length distribution range of 1000–5000 nm [Fig. 7(b)], (2) s-B2 precipitates with a diameter distribution range of 200–900 nm [Fig. 8(a)], and (3) t-B2 precipitates with a diameter distribution range of 5–50 nm [Fig. 8(b)]. The average particle size of these B2 precipitates in each HEA is calculated and summarized in Table 4. One can note that the average diameter of the three B2 precipitates decreases with increasing the Al content (from A5 to A8 alloys). Depending on Santodonato et al.'s research [58], the Al-Ni and Cr-Fe atomic pairs in the liquid phase of Al-TMs HEA systems are much more likely to be found as the nearest-neighbour pairs, which can be viewed as precursors for nucleating the segregated Al-Ni-enriched B2 phase and Cr-Fe-enriched BCC phase. Thus, increasing the Al content can increase the nucleation rate of the Al-Ni phase, which can increase the number density of the B2 precipitates and refine the particle size. Apart from the difference of the average particle size, these coherent B2 precipitates also display three different morphologies. The equilibrium shape of a precipitate is determined by minimizing the sum of the interfacial and elastic energies [59,60]. The symmetry of the precipitates (from t-B2 to s-B2 to p-B2 structures) is gradually reduced.

3.3. Mechanical properties

Compression and hardness tests were conducted to examine the mechanical properties of the current HEAs. The compression true stress-strain curves and Vickers hardness tested at room temperature are depicted in Fig. 9. With increasing the Al content, the yield strength increases from 1091 MPa (the A5 alloy) to 1200 MPa (the A8 alloy). A high compression plasticity (> 45%) in these designed HEAs is observed, which is attributed to the strong work-hardening ability. It is apparent that these trimodal HEAs exhibit superior compressive mechanical properties. The Vickers hardness also shows a slight increase from 353 HV (A5 alloy) to 386 HV (A8 alloy). It is noted that the

Table 3
Chemical compositions and crystal structures of different phases in the $Al_xCrFeMnNi$ HEAs by EDS (at.%).

Alloys	Phases	Chemical compositions (at.%)				
		Al	Cr	Mn	Fe	Ni
A5	BCC (matrix)	6.55 ± 0.39	26.53 ± 0.45	22.52 ± 0.41	24.31 ± 0.35	20.09 ± 0.58
	t-B2	13.62 ± 0.53	19.54 ± 0.48	21.01 ± 0.61	20.02 ± 0.52	25.81 ± 0.46
	s-B2	13.38 ± 0.47	20.98 ± 0.51	20.28 ± 0.43	19.74 ± 0.39	25.62 ± 0.33
	p-B2	13.72 ± 0.46	20.22 ± 0.43	20.34 ± 0.53	20.37 ± 0.35	25.35 ± 0.41
A6	BCC (matrix)	7.54 ± 0.49	26.22 ± 0.60	22.08 ± 0.58	25.78 ± 0.43	18.38 ± 0.23
	t-B2	16.54 ± 0.57	18.97 ± 0.44	19.50 ± 0.52	19.55 ± 0.38	25.44 ± 0.63
	s-B2	16.48 ± 0.64	18.64 ± 0.55	19.69 ± 0.47	18.75 ± 0.34	26.44 ± 0.47
	p-B2	16.69 ± 0.34	19.01 ± 0.44	20.20 ± 0.36	18.32 ± 0.37	25.78 ± 0.43
A7	BCC (matrix)	8.93 ± 0.58	26.70 ± 0.62	21.57 ± 0.46	26.74 ± 0.56	16.06 ± 0.50
	t-B2	18.93 ± 0.64	17.01 ± 0.61	19.88 ± 0.59	19.52 ± 0.49	24.66 ± 0.57
	s-B2	18.22 ± 0.44	17.45 ± 0.56	19.84 ± 0.61	18.81 ± 0.38	25.68 ± 0.59
	p-B2	18.87 ± 0.38	18.04 ± 0.44	19.35 ± 0.52	17.89 ± 0.45	25.85 ± 0.50
A8	BCC (matrix)	10.06 ± 0.61	27.49 ± 0.58	20.94 ± 0.57	27.50 ± 0.49	14.01 ± 0.55
	t-B2	20.30 ± 0.54	17.29 ± 0.64	19.57 ± 0.39	18.30 ± 0.52	24.54 ± 0.58
	s-B2	20.06 ± 0.58	17.23 ± 0.64	18.96 ± 0.46	17.26 ± 0.50	26.29 ± 0.60
	p-B2	21.71 ± 0.48	16.18 ± 0.59	18.46 ± 0.39	17.15 ± 0.34	26.50 ± 0.55

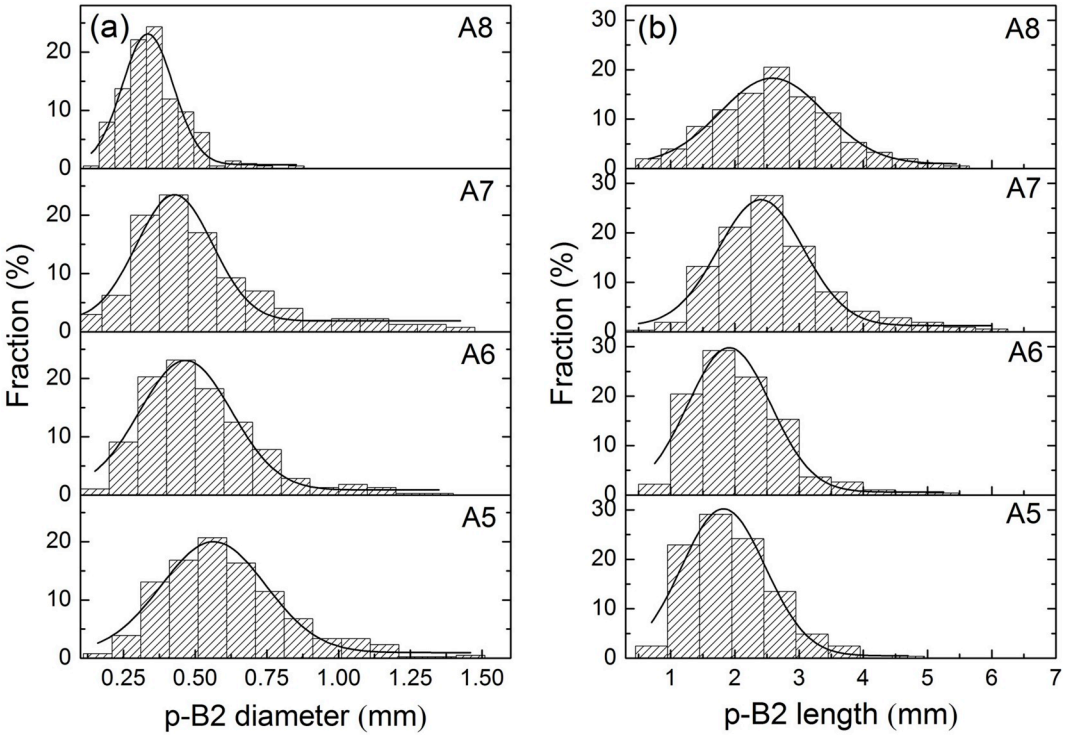

Fig. 7. The distributions of diameter (a) and length (b) for the p-B2 precipitates of the current four trimodal HEAs.

relationship between the microhardness and the yield strength obeys well the Tabor relationship [61], namely $HV = c\sigma_y$. The calculated proportional coefficient, *c*, of the four HEAs is about 3.2, which is similar to that in these conventional steels, $(FeCoNiCrMn)_{100-x}Al_x$ [46], and Al-Ni-Co-Fe-Cr HEAs [48]. The nanoindentation tests conducted in the DR region and ID region of the A8 alloy showed a small difference in nanohardness values, ~5.3 GPa and ~5.7 GPa, respectively.

3.4. Strengthening mechanisms

For the present trimodal HEAs, many strengthening mechanisms are active concurrently, including the solid-solution strengthening ($\Delta\sigma_S$), precipitation strengthening ($\Delta\sigma_P$), and precipitate size strengthening ($\Delta\sigma_G$). The increase of the yield strength is a summation of the individual contributions, given by:

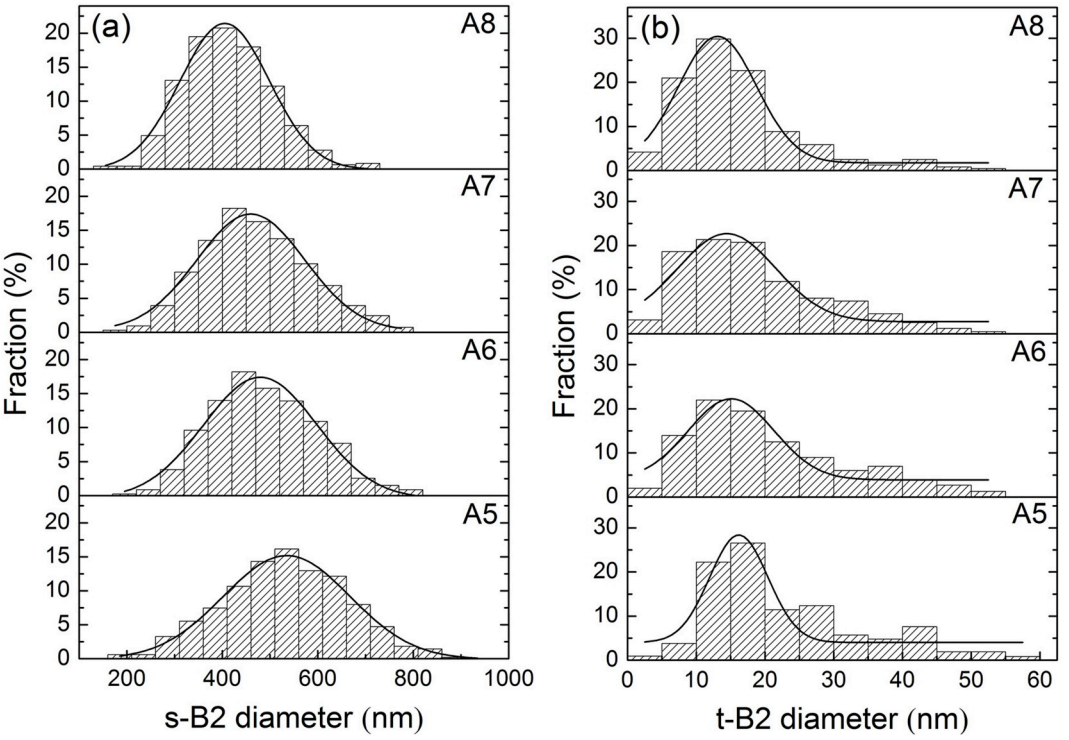

Fig. 8. Particle-size distributions for the s-B2 precipitates (a) and t-B2 precipitates (b) of the current four trimodal HEAs.

Table 4
Data summary of the three ordered B2 precipitates and BCC matrix in the designed trimodal HEAs, including the lattice constant (α), Burger's vector (b), lattice misfit (ε), the average size (r) of the B2 precipitate, the length (l) of the rod-shaped p-B2 precipitate, and the average volume fraction of B2 precipitates in the alloy (f) and in the ID or DR region ($f_{ID/DR}$).

Alloys	Phases	α (Å)	b (Å)	ε (%)	r (nm)	l (μm)	$f_{ID/DR}$ (%)	f (%)
A5	BCC (matrix)	2.8857	2.4991	–	–	–	–	19.2
	p-B2	2.9011	2.5124	0.53	580	1.83	81.5	15.3
	s-B2	2.8986	2.5103	0.45	530	–	59	47.8
	t-B2	2.8978	2.5096	0.42	22	–	53	17.6
A6	BCC (matrix)	2.8878	2.5009	–	–	–	–	18.9
	p-B2	2.9025	2.5136	0.50	510	2.04	80	26.8
	s-B2	2.8995	2.5110	0.40	485	–	60	39.9
	t-B2	2.8998	2.5113	0.41	21	–	54	14.4
A7	BCC (matrix)	2.8962	2.5082	–	–	–	–	22.5
	p-B2	2.9098	2.5199	0.47	480	2.30	81	33.0
	s-B2	2.9075	2.5180	0.39	450	–	63	33.6
	t-B2	2.9078	2.5182	0.40	20	–	55	10.9
A8	BCC (matrix)	2.9002	2.5116	–	–	–	–	16.5
	p-B2	2.9128	2.5226	0.43	395	2.52	81.5	38.0
	s-B2	2.9123	2.5221	0.41	415	–	65	34.7
	t-B2	2.9114	2.5213	0.39	17	–	58	10.8

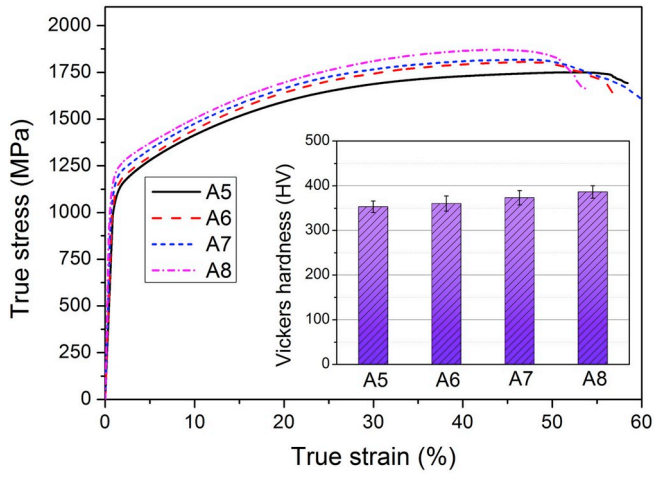

Fig. 9. Compression true stress-strain curves and the Vickers hardness of the four HEAs.

$$\sigma_Y = \sigma_0 + \Delta\sigma_S + \Delta\sigma_P + \Delta\sigma_G \quad (1)$$

where σ_0 is the intrinsic strength of the present HEAs. Predictions of the contribution of each strengthening mechanism for these trimodal HEAs are described below.

3.4.1. Solid-solution strengthening

In traditional alloys, solid-solution strengthening arises from the interactions of the solute atoms and moving dislocations, as described by Fleischer [62] and Labusch [63]. However, for the multi-component HEAs, viewed as specific cases of non-dilute random solid solutions, the "solvent" and "solute" terms lose their conventional meanings. Therefore, the Fleischer's and Labusch's approaches are not appropriate for the multi-component systems. Gypen and Deruyttere [64] proposed a new methodology to calculate the solution strengthening in multi-component alloys, which can be expressed as:

$$\Delta\sigma_s = \left(\sum_i B_i^{3/2} X_i\right)^{2/3} \quad (2)$$

where B_i is the hardening parameter of the ith element, and X_i is its atomic fraction. This approach has been successfully applied in recent studies of multi-component Mg alloys [65] and HEAs [66].

$$B_i = 3\mu\varepsilon_i^{4/3} Z \;;\; \varepsilon_i = \xi\left(\eta'^{2}_i + \kappa^2\delta_i^2\right)^{1/2} \quad (3)$$

Here, μ is the shear modulus of the alloy, Z is a fitting constant [65], and ε_i is a function of the elastic misfit η'_i and the atomic-size misfit δ_i, $\xi = 4$ for the BCC metals, and $\kappa = 16$ is taken for Labusch's approximation.

$$\eta'_i = \frac{\eta_i}{1 + 0.5|\eta_i|};\; \eta_i = \frac{d\mu}{dX_i}\frac{1}{\mu} \quad (4)$$

where the modulus misfit, η_i, for multi-component alloys can be approximated by Ref. [66]:

$$\eta_i = 2\left(\frac{\mu_i - \mu_{HEA}}{\mu_i + \mu_{HEA}}\right);\; \mu_{HEA} = \sum_i^n X_i\mu_i \quad (5)$$

where μ_i is the shear modulus of the ith element (see Table 1 or [67]), and μ_{HEA} is the shear modulus of the HEA. The atomic-size misfit, δ_i, is described as:

$$\delta_i = \frac{d\alpha}{dX_i}\frac{1}{\alpha} \quad (6)$$

where α is the cell parameter of the alloy. The atomic-size misfit for HEAs is calculated, employing the method as in Ref. [66]. The detailed equations are given in Appendix A.

The solid-solution strengthening theory for the multicomponent B2 phase is not available in the literature. Here, we use the above approach as estimates for these B2 precipitates. For the present trimodal HEAs, solid-solution strengthening in both the B2 precipitates and BCC phase should be included in the calculations of the overall yield strength.

$$\Delta\sigma_S = f_{BCC} * \Delta\sigma_s^{BCC} + f_{t-B2} * \Delta\sigma_s^{t-B2} + f_{s-B2} * \Delta\sigma_s^{s-B2} + f_{p-B2} * \Delta\sigma_s^{p-B2} \quad (7)$$

where f_{BCC}, $f_{t\text{-}B2}$, $f_{s\text{-}B2}$, and $f_{p\text{-}B2}$ are the volume fractions of BCC, t-B2, s-B2, and p-B2 precipitates, respectively, as listed in Table 4. The calculated values of $\Delta\sigma_S$ for the current HEAs are summarized in Table 5.

3.4.2. Precipitation strengthening

Based on the interaction between the dislocations and precipitates, the precipitation-strengthening mechanism can be either precipitate shearing or Orowan by-passing. Generally, the shearing mechanism occurs when the precipitates are coherent and small, while the Orowan mechanism would dominate, when the precipitates are large or incoherent with the matrix.

For the shearing mechanism, there are three contributing factors to the increase in the yield strength, including the coherency strengthening ($\Delta\sigma_{cs}$), modulus-mismatch strengthening ($\Delta\sigma_{ms}$), and order strengthening ($\Delta\sigma_{os}$). The former two factors ($\Delta\sigma_{cs}$ and $\Delta\sigma_{ms}$) make contributions prior to the shearing of the precipitates, while the latter one ($\Delta\sigma_{os}$) contributes during shearing. In this case, the total strength increment from the precipitate shearing is determined by the larger of $\Delta\sigma_{cs} + \Delta\sigma_{ms}$ or $\Delta\sigma_{os}$. The equations of the three factors are expressed as

Table 5
Summary of the increments of the yield strength contributions from the different strengthening mechanisms, including the solid-solution strengthening ($\Delta\sigma_S$), precipitate-shearing strengthening for t-B2 precipitates ($\Delta\sigma t\text{-}B2\ P$), Orowan by-passing strengthening for s-B2 precipitates ($\Delta\sigma s\text{-}B2\ P$), and precipitate size strengthening ($\Delta\sigma_G$). The units of the values in this table are MPa.

	A5	A6	A7	A8
$\Delta\sigma_S$	111	115	118	122
$\Delta\sigma t\text{-}B2\ P$	290	233	193	168
$\Delta\sigma s\text{-}B2\ P$	319	297	330	355
$\Delta\sigma_G$	127	235	287	359

[68–70]:

$$\Delta\sigma_{cs} = M * \alpha_\varepsilon * (G\varepsilon_c)^{3/2} * \left(\frac{rf}{0.5Gb}\right)^{1/2} \quad (8)$$

$$\Delta\sigma_{ms} = M * 0.0055 * (\Delta G)^{3/2} * \left(\frac{2f}{G}\right)^{1/2} * \left(\frac{r}{b}\right)^{\frac{3m}{2}-1} \quad (9)$$

$$\Delta\sigma_{os} = M * 0.81 * \frac{\gamma_{APB}}{2b} * \left(\frac{3\pi f}{8}\right)^{1/2} \quad (10)$$

where M (= 2.73 for the BCC structure) is a Taylor factor, α_ε = 2.6 (a constant), $\varepsilon_c = 2\varepsilon/3$ is the constrained lattice misfit, m = 0.85, G is the shear modulus of the matrix, ΔG is the shear-modulus mismatch between the matrix and precipitate, r, f, $b = \sqrt{3}\alpha/2$, and γ_{APB} are, respectively, the average size, volume fraction, Burgers vector, and anti-phase boundary energy of the precipitates. For the present HEAs, the strength increment can be obtained using γ_{APB} = 0.25 J/m^2 [71], G = 83 GPa (for α-Fe) [72], and ΔG = 83 - 80 GPa (the shear modulus of the B2-NiAl phase is G = 80 GPa [73]).

For the Orowan mechanism, the strength increment due to dislocation looping around the precipitates is given by Refs. [74,75]:

$$\Delta\sigma_{or} = \frac{0.4MGb}{\pi\sqrt{1-\upsilon}} * \frac{\ln\left(\frac{2r\sqrt{2/3}}{b}\right)}{\lambda} \quad (11)$$

where υ = 0.3 is the Poisson's ratio of the BCC HEAs [48], and λ is the inter-precipitate spacing, which is defined as [76]:

$$\lambda = \left(\sqrt{\frac{3\pi}{4f}} - 1.64\right)r \quad (12)$$

As suggested in Refs. [48,77], the shearing and Orowan by-passing mechanisms are in parallel and independent to each other. The strengthening is given by the smaller of the two mechanisms. For the t-B2 precipitates of the current HEAs, strengthening caused by the two mechanisms are plotted as a function of r with a fixed f, as shown in Fig. 10. This figure predicts that $\Delta\sigma_{os}$ is dominant for r less than ~20 nm, $\Delta\sigma_{cs} + \Delta\sigma_{ms}$ for r between 20 nm and r_0, and $\Delta\sigma_{or}$ for r larger than r_0. The values of the critical size (r_0) for the strengthening mechanism changing from the precipitate shearing to Orowan mechanism for the t-B2 precipitates are 75 nm (A5 alloy), 79 nm (A6 alloy), 84 nm (A7 alloy), and 92 nm (A8 alloy), respectively. The results are consistent with some other B2/BCC HEAs with coherent B2 precipitates, such as $Al_{12.5}Ni_{17.5}Co_{17.5}Fe_{35}Cr_{17.5}$ (r_0 = 60 nm, f = 0.4) [48], $Al_{12.5}Ni_{17.5}Co_{17.5}Fe_{17.5}Cr_{35}$ (r_0 = 88 nm, f = 0.55) [48], and $Al_{0.7}CoCrFe_2Ni$ (r_0 = 71 nm, f = 0.4) [78]. The particle size of the t-B2 in each alloy is smaller than 50 nm and their strength is thus predicted

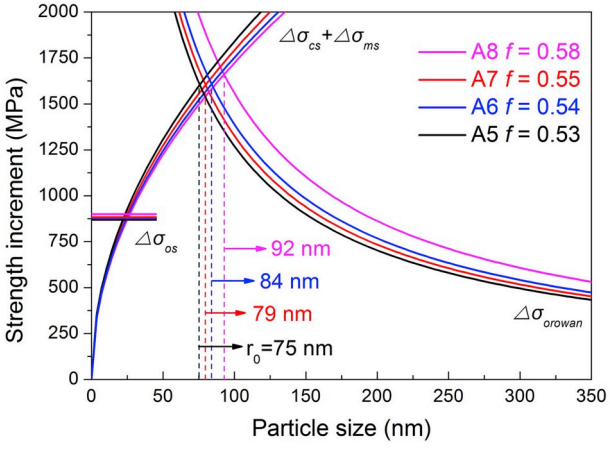

Fig. 10. Computations of $\Delta\sigma_{os}$, $\Delta\sigma_{cs} + \Delta\sigma_{ms}$, and $\Delta\sigma_{or}$ as a function of the particle size, r, for the current HEAs.

to be controlled by the shearing mechanism. The size parameters of the t-B2 precipitates are listed in Table 4. After the calculation, the values of $\Delta\sigma_{cs} + \Delta\sigma_{ms}$ for the A5, A6, A7, and A8 alloys are 855 MPa, 820 MPa, 786 MPa, and 703 MPa, respectively. The values of $\Delta\sigma_{os}$ for the A5, A6, A7, and A8 alloys are 870 MPa, 878 MPa, 883 MPa, and 900 MPa, respectively. The strength increment from the coherency and modulus-mismatch strengthening is noted to be less than that from order strengthening (i.e., $\Delta\sigma_{cs} + \Delta\sigma_{ms} < \Delta\sigma_{os}$), suggesting the order strengthening dominates the shearing mechanism in the current HEAs.

For the larger s-B2 precipitates ($r \approx$ 450 nm), it is difficult for the dislocations to shear the precipitates ($\Delta\sigma_{cs} + \Delta\sigma_{ms} > \Delta\sigma_{or}$). The Orowan mechanism will dominate in the s-B2 precipitates. The values of b, f, and r for the s-B2 precipitates are shown in Table 4. Through the above two Equations (11) and (12), the strengthening increment from the Orowan mechanism in each alloy can be obtained.

Finally, the precipitation strengthening resulting from the precipitate shearing (t-B2 precipitates) and Orowan by-passing (s-B2 precipitates) mechanisms in the current HEAs can be written as:

$$\Delta\sigma_P = \Delta\sigma_P^{t-B2} + \Delta\sigma_P^{s-B2} = (1 - f_{DR}^{s-B2})f_{DR}\Delta\sigma_{os}^{t-B2} + f_{DR}\Delta\sigma_{or}^{s-B2} \quad (13)$$

Here, f_{DR} is the volume fraction of the DR region (see Fig. 3), f_{DR}^{s-B2} is the volume fraction of the s-B2 precipitates in the DR region (Table 4), and $(1 - f_{DR}^{s-B2})$ is the volume fraction of the t-B2 + BCC matrix in the DR region. The calculated values for the precipitation strengthening in each HEA are presented in Table 5.

3.4.3. Precipitate size strengthening

The Orowan equations are not suitable for the p-B2 precipitates due to the high length-to-diameter ratio for these precipitates. However, the precipitate size strengthening is a feasible method of estimating the strength contribution from these large primary precipitates in ID regions, just as shown in Ref. [51]. The strengthening mechanism is attributed to the existence of a high volumetric density of p-B2/BCC grain boundaries as sources of dislocations and barriers to deformation. In principle, this strengthening mechanism obeys the Hall-Petch relationship [79]: $\Delta\sigma = Kd^{-1/2}$, where K is the Hall-Petch coefficient, and d is the average grain size. For the present HEAs, the ID regions possess a high density of grain boundaries created by the p-B2 precipitates. To account for the geometric anisotropy, the strength increment from these p-B2 precipitates is given by:

$$\Delta\sigma_G = \frac{2}{3}f_{ID}Kr^{-1/2} + \frac{1}{3}f_{ID}Kl^{-1/2} \quad (14)$$

where f_{ID} is the volume fraction of the ID region (see Fig. 3), K is taken as 0.6 MPa m$^{1/2}$ (for α-Fe) [80,81], r and l are the diameter and length of the p-B2 precipitates (Table 4). This equation is an approximate estimation of the p-B2 precipitates contribution on the overall strength. The calculated values of the strength increments for each HEA are shown in Table 5.

Based on the discussion above, the predicted values of the strength contributions from each individual mechanism are summarized in Table 5. One can note that the three kinds of B2 precipitates offer the largest strength increment for the present trimodal HEAs. The precipitation strengthening is the dominate mechanism in the current HEAs.

4. Conclusions

In this study, we have successfully fabricated a series of novel $Al_xCrFeMnNi$ (x = 0.5–0.8) HEAs with trimodal distributions of coherent B2 precipitates. The microstructural evolution, phase transition, mechanical properties, and strengthening mechanisms of the designed HEAs have been studied systematically. The following conclusions are drawn:

(1) The SEM and TEM analyses indicate that the ordered B2

precipitates with trimodal distributions coherently distribute within the disordered BCC solid-solution matrix for the designed HEAs. The trimodal-size distributions of the B2 precipitates contain: (a) the t-B2 precipitates with a mean diameter of ~20 nm, (b) the s-B2 precipitates with a mean diameter of ~450 nm located in the DR region, and (c) the p-B2 precipitates with a mean length of ~2 μm located in the ID region. Adjusting the Al content does not change the phase constitutions and the trimodal microstructures, but the average size and volume fraction of these precipitates show slight changes.

(2) These trimodal BCC/B2 HEAs exhibit a good combination of the high compressive yield strength (1091–1200 MPa) and large plasticity (> 45%).

(3) Using extant strengthening theories, the strengthening mechanisms of the designed HEAs are quantitatively analyzed in terms of the solid-solution strengthening, precipitation strengthening, and precipitate size strengthening. The large strength contributions result from the three kinds of B2 precipitates. Precipitation strengthening mechanisms play major roles in strengthening the HEAs.

Acknowledgments

Gong Li would like to acknowledge the Basic Research Project in the Hebei Province (Grant No. A2016203382), and the support from the National Science Foundation of China (Grant No. 11674274). Peng Fei Yu would like to acknowledge the National Natural Science Funds of China (Grant No. 51601166).

Appendix A

For the multi-component HEAs, there is a variation of the interatomic distance in the crystal lattice around its mean unit cell parameter [66]. The atomic-size misfit is related to the crystal-lattice distortion by the constituent elements. The interatomic spacing between atoms (s) is proportional to the cell parameter (α), as follows:

$$s = \psi\alpha \tag{A.1}$$

where ψ is a packing factor for different crystal structures, $\psi = \sqrt{3}/2$ for the BCC alloys, and $\psi = 1/\sqrt{2}$ for FCC alloys. Thus, Eq. (6) can be converted to:

$$\delta_i = \frac{\mathrm{d}s}{\mathrm{d}X_i}\frac{1}{s} \tag{A.2}$$

The average interatomic spacing, s^{ave}, of the alloy is approximated by:

$$s^{ave} = \sum_i^n \sum_j^n s_{ij}X_iX_j = (X_1, \cdots, X_n)\begin{pmatrix} s_{11} & s_{12} & \cdots & s_{1n} \\ s_{21} & s_{22} & \cdots & s_{2n} \\ \vdots & \cdots & \ddots & \vdots \\ s_{n1} & s_{n2} & \cdots & s_{nn} \end{pmatrix}\begin{pmatrix} X_1 \\ \vdots \\ X_n \end{pmatrix} \tag{A.3}$$

where s_{ij} is the interatomic spacing between atoms of types, i and j, s_{ii} and s_{jj} are the interatomic spacings of pure elements, i and j. The average interatomic spacing, s_{bin}^{ave}, of the binary alloy can be calculated via the cell parameter, α_{bin}, in Eq. (A.4). Thus, the interatomic spacing, s_{ij}, can be obtained, using the form of Eq. (A.3) in the binary system, which now becomes:

$$s_{bin}^{ave} = \psi\alpha_{bin} = s_{ii}X_i^2 + 2s_{ij}X_iX_j + s_{jj}X_j^2 \tag{A.4}$$

The calculation of the unit-cell parameter, α_{bin}, of a binary system is based on the Lubarda's approach [67], which is expressed as:

$$\alpha_{bin} = \left(\alpha^3 + 4\pi R^3 X_i \frac{n}{\zeta}\gamma C\right)^{1/3} \tag{A.5}$$

where α is the solvent atom unit cell parameter, R is its Wigner-Seitz atomic radius, n is the number of atoms per unit cell, and the atomic volume is $\zeta\alpha^3/n$, ζ is a constant based on the crystal structure, and the parameters, γ and C, are defined by:

$$\gamma = 1 + \frac{4\mu}{3k};\ C = \frac{1}{\gamma_i}\frac{R_i - R}{R};\ C = \frac{1}{\gamma_i}\frac{R_i - R}{R} \tag{A.6}$$

where μ and μ_i are the shear moduli of the solvent and solute, and k and k_i are the bulk moduli of the solvent and solute, respectively. The corresponding values of the above parameters for the constituent elements in the present HEAs are shown in Ref. [67]. Finally, the atomic-size misfit by each element can be obtained through Eqs. (A.2) and (A.3).

References

[1] J.W. Yeh, S.K. Chen, S.J. Lin, J.Y. Gan, T.S. Chin, T.T. Shun, C.H. Tsau, S.Y. Chang, Nanostructured high-entropy alloys with multiple principal elements: novel alloy design concepts and outcomes, Adv. Eng. Mater. 6 (5) (2004) 299–303.
[2] B. Cantor, I.T.H. Chang, P. Knight, A.J.B. Vincent, Microstructural development in equiatomic multicomponent alloys, Mater. Sci. Eng. 375–377 (1) (2004) 213–218.
[3] J.W. Yeh, Overview of High-Entropy Alloys, Springer International Publishing, 2016.
[4] Y. Zhang, T.T. Zuo, Z. Tang, M.C. Gao, K.A. Dahmen, P.K. Liaw, Z.P. Lu, Microstructures and properties of high-entropy alloys, Prog. Mater. Sci. 61 (2014) 1–93.
[5] D.B. Miracle, O.N. Senkov, A critical review of high entropy alloys and related concepts, Acta Mater. 122 (2017) 448–511.
[6] M. Feuerbacher, M. Heidelmann, C. Thomas, Hexagonal high-entropy alloys, Mater Res Lett 3 (1) (2015) 1–6.
[7] K.M. Youssef, A.J. Zaddach, C. Niu, D.L. Irving, C.C. Koch, A novel low-density, high-hardness, high-entropy alloy with close-packed single-phase nanocrystalline structures, Mater Res Lett 3 (2) (2015) 95–99.
[8] Y.F. Ye, Q. Wang, J. Lu, C.T. Liu, Y. Yang, High-entropy alloy: challenges and prospects, Mater. Today 19 (6) (2016) 349–362.
[9] Z. Tang, T. Yuan, C.W. Tsai, J.W. Yeh, C.D. Lundin, P.K. Liaw, Fatigue behavior of a wrought $Al_{0.5}$CoCrCuFeNi two-phase high-entropy alloy, Acta Mater. 99 (2015) 247–258.
[10] M.A. Hemphill, T. Yuan, G.Y. Wang, J.W. Yeh, C.W. Tsai, A. Chuang, P.K. Liaw, Fatigue behavior of $Al_{0.5}$CoCrCuFeNi high entropy alloys, Acta Mater. 60 (16) (2012) 5723–5734.
[11] K.V.S. Thurston, B. Gludovatz, A. Hohenwarter, G. Laplanche, E.P. George, R.O. Ritchie, Effect of temperature on the fatigue-crack growth behavior of the high-entropy alloy CrMnFeCoNi, Intermetallics 88 (2017) 65–72.
[12] P.Y. Chen, L. Chanho, S.Y. Wang, S. Mohsen, J.J. Lewandowski, K.A. Dahmen, H.L. Jia, X. Xie, B.L. Chen, Y. Jien-Wei, Fatigue behavior of high-entropy alloys:A review, Sci. China Technol. Sci. 61 (2) (2018) 168–178.
[13] W. Kai, C.C. Li, F.P. Cheng, K.P. Chu, R.T. Huang, L.W. Tsay, J.J. Kai, Air-oxidation of FeCoNiCr-based quinary high-entropy alloys at 700–900 °C, Corros. Sci. 121

(2017) 116–125.
[14] Y. Shi, B. Yang, X. Xie, J. Brechtl, K.A. Dahmen, P.K. Liaw, Corrosion of $Al_xCoCrFeNi$ high-entropy alloys: Al-content and potential scan-rate dependent pitting behavior, Corros. Sci. 119 (2017) 33–45.
[15] Y. Shi, L. Collins, R. Feng, C. Zhang, N. Balke, P.K. Liaw, B. Yang, Homogenization of $Al_xCoCrFeNi$ high-entropy alloys with improved corrosion resistance, Corros. Sci. 133 (2018) 120–131.
[16] B. Gorr, M. Azim, H.J. Christ, T. Mueller, D. Schliephake, M. Heilmaier, Phase equilibria, microstructure, and high temperature oxidation resistance of novel refractory high-entropy alloys, J. Alloy. Comp. 624 (2015) 270–278.
[17] Y. Shi, B. Yang, P.K. Liaw, Corrosion-resistant high-entropy alloys: a review, Metals 7 (2) (2017) 43.
[18] C. Lu, L. Niu, N. Chen, K. Jin, T. Yang, P. Xiu, Y. Zhang, F. Gao, H. Bei, S. Shi, Enhancing radiation tolerance by controlling defect mobility and migration pathways in multicomponent single-phase alloys, Nat. Commun. 7 (2016) 13564.
[19] N.A.P. Kiran Kumar, C. Li, K.J. Leonard, H. Bei, S.J. Zinkle, Microstructural stability and mechanical behavior of FeNiMnCr high entropy alloy under ion irradiation, Acta Mater. 113 (2016) 230–244.
[20] J. Guo, H. Wang, F.V. Rohr, Z. Wang, S. Cai, Y. Zhou, K. Yang, A. Li, S. Jiang, Q. Wu, R.J. Cava, L. Sun, Robust zero resistance in a superconducting high-entropy alloy at pressures up to 190 GPa, Proc. Natl. Acad. Sci. Unit. States Am. 114 (50) (2017) 13144–13147.
[21] P. Koželj, S. Vrtnik, A. Jelen, S. Jazbec, Z. Jagličić, S. Maiti, M. Feuerbacher, W. Steurer, J. Dolinšek, Discovery of a superconducting high-entropy alloy, Phys. Rev. Lett. 113 (10) (2014) 107001.
[22] H. Chen, A. Kauffmann, B. Gorr, D. Schliephake, C. Seemüller, J. Wagner, H.J. Christ, M. Heilmaier, Microstructure and mechanical properties at elevated temperatures of a new Al-containing refractory high-entropy alloy Nb-Mo-Cr-Ti-Al, J. Alloy. Comp. 661 (2016) 206–215.
[23] N.K. Kumar, C. Li, K. Leonard, H. Bei, S. Zinkle, Microstructural stability and mechanical behavior of FeNiMnCr high entropy alloy under ion irradiation, Acta Mater. 113 (2016) 230–244.
[24] J. Liu, X. Guo, Q. Lin, Z. He, X. An, L. Li, P.K. Liaw, X. Liao, L. Yu, J. Lin, Excellent ductility and serration feature of metastable CoCrFeNi high-entropy alloy at extremely low temperatures, Sci. China. Mater. 62 (6) (2019) 853–863.
[25] J. Moon, S.I. Hong, J.W. Bae, J.W. Jang, D. Yim, H.S. Kim, On the strain rate-dependent deformation mechanism of CoCrFeMnNi high-entropy alloy at liquid nitrogen temperature, Mater. Res. Lett. 5 (7) (2017) 472–477.
[26] J.Y. He, H. Wang, H.L. Huang, X.D. Xu, M.W. Chen, Y. Wu, X.J. Liu, T.G. Nieh, K. An, Z.P. Lu, A precipitation-hardened high-entropy alloy with outstanding tensile properties, Acta Mater. 102 (2016) 187–196.
[27] Y.L. Zhao, T. Yang, J.H. Zhu, D. Chen, Y. Yang, A. Hu, C.T. Liu, J.J. Kai, Development of high-strength Co-free high-entropy alloys hardened by nanosized precipitates, Scripta Mater. 148 (2018) 51–55.
[28] T. Yang, Y.L. Zhao, Y. Tong, Z.B. Jiao, J. Wei, J.X. Cai, X.D. Han, D. Chen, A. Hu, J.J. Kai, K. Lu, Y. Liu, C.T. Liu, Multicomponent intermetallic nanoparticles and superb mechanical behaviors of complex alloys, Science 362 (6417) (2018) 933–937.
[29] B. Schuh, F. Mendez-Martin, B. Volker, E.P. George, H. Clemens, R. Pippan, A. Hohenwarter, Mechanical properties, microstructure and thermal stability of a nanocrystalline CoCrFeMnNi high-entropy alloy after severe plastic deformation, Acta Mater. 96 (2015) 258–268.
[30] H. Shahmir, T. Mousavi, J. He, Z. Lu, M. Kawasaki, T.G. Langdon, Microstructure and properties of a CoCrFeNiMn high-entropy alloy processed by equal-channel angular pressing, Mater. Sci. Eng., A 705 (2017) 411–419.
[31] H. Shiratori, T. Fujieda, K. Yamanaka, Y. Koizumi, K. Kuwabara, T. Kato, A. Chiba, Relationship between the microstructure and mechanical properties of an equiatomic AlCoCrFeNi high-entropy alloy fabricated by selective electron beam melting, Mater. Sci. Eng. 656 (2016) 39–46.
[32] Y. Ma, B. Jiang, C. Li, Q. Wang, C. Dong, P.K. Liaw, F. Xu, L. Sun, The BCC/B2 morphologies in $Al_xNiCoFeCr$ high-entropy alloys, Metals 7 (2) (2017) 57.
[33] S. Xia, X. Yang, M. Chen, T. Yang, Y. Zhang, The Al effects of Co-free and V-containing high-entropy alloys, Metals 7 (1) (2017) 18.
[34] L. Lu, Y. Shen, X. Chen, L. Qian, K. Lu, Ultrahigh strength and high electrical conductivity in copper, Science 304 (5669) (2004) 422–426.
[35] K. Lu, L. Lu, S. Suresh, Strengthening materials by engineering coherent internal boundaries at the nanoscale, Science 324 (5925) (2009) 349–352.
[36] S. Jiang, H. Wang, Y. Wu, X. Liu, H. Chen, M. Yao, B. Gault, D. Ponge, D. Raabe, A. Hirata, M. Chen, Y. Wang, Z. Lu, Ultrastrong steel via minimal lattice misfit and high-density nanoprecipitation, Nature 544 (7651) (2017) 460–464.
[37] Z. Fu, L. Jiang, J.L. Wardini, B.E. MacDonald, H. Wen, W. Xiong, D. Zhang, Y. Zhou, T.J. Rupert, W. Chen, A high-entropy alloy with hierarchical nanoprecipitates and ultrahigh strength, Science advances 4 (10) (2018) eaat8712.
[38] N. Stepanov, D. Shaysultanov, M. Tikhonovsky, S. Zherebtsov, Structure and high temperature mechanical properties of novel non-equiatomic Fe-(Co, Mn)-Cr-Ni-Al-(Ti) high entropy alloys, Intermetallics 102 (2018) 140–151.
[39] D. Shaysultanov, G. Salishchev, Y.V. Ivanisenko, S. Zherebtsov, M. Tikhonovsky, N. Stepanov, Novel $Fe_{36}Mn_{21}Cr_{18}Ni_{15}Al_{10}$ high entropy alloy with bcc/B2 dual-phase structure, J. Alloy. Comp. 705 (2017) 756–763.
[40] C. Yang, L.M. Kang, X.X. Li, W.W. Zhang, D.T. Zhang, Z.Q. Fu, Y.Y. Li, L.C. Zhang, E.J. Lavernia, Bimodal titanium alloys with ultrafine lamellar eutectic structure fabricated by semi-solid sintering, Acta Mater. 132 (2017) 491–502.
[41] Q. Wang, C. Ji, Y. Wang, J. Qiang, C. Dong, β-Ti alloys with low Young's moduli interpreted by cluster-plus-glue-atom model, Metall. Mater. Trans. 44 (4) (2013) 1872–1879.
[42] H.L. Hong, Q. Wang, C. Dong, P.K. Liaw, Understanding the Cu-Zn brass alloys using a short-range-order cluster model: significance of specific compositions of industrial alloys, Sci. Rep. 4 (2) (2014) 7065.
[43] Y. Ma, Q. Wang, C. Li, L.J. Santodonato, M. Feygenson, C. Dong, P.K. Liaw, Chemical short-range orders and the induced structural transition in high-entropy alloys, Scripta Mater. 144 (2018) 64–68.
[44] A. Takeuchi, A. Inoue, Classification of bulk metallic glasses by atomic size difference, heat of mixing and period of constituent elements and its application to characterization of the main alloying element, Mater. Trans. 46 (12) (2006) 2817–2829.
[45] Y.F. Kao, T.J. Chen, S.K. Chen, J.W. Yeh, Microstructure and mechanical property of as-cast, -homogenized, and -deformed $Al_xCoCrFeNi$ ($0 \le x \le 2$) high-entropy alloys, J. Alloy. Comp. 488 (1) (2009) 57–64.
[46] J.Y. He, W.H. Liu, H. Wang, Y. Wu, X.J. Liu, T.G. Nieh, Z.P. Lu, Effects of Al addition on structural evolution and tensile properties of the FeCoNiCrMn high-entropy alloy system, Acta Mater. 62 (1) (2014) 105–113.
[47] J.M. Wu, S.J. Lin, J.W. Yeh, S.K. Chen, Y.S. Huang, H.C. Chen, Adhesive wear behavior of $Al_xCoCrCuFeNi$ high-entropy alloys as a function of aluminum content, Wear 261 (5–6) (2006) 513–519.
[48] Y. Ma, Q. Wang, B.B. Jiang, C.L. Li, J.M. Hao, X.N. Li, C. Dong, T.G. Nieh, Controlled formation of coherent cuboidal nanoprecipitates in body-centered cubic high-entropy alloys based on $Al_2(Ni,Co,Fe,Cr)_{14}$ compositions, Acta Mater. 147 (2018) 213–225.
[49] R. Megargle, ASTM (American Society for Testing and Materials) standards for medical computing, Comput. Healthc. 11 (2) (1990) 25.
[50] Y. Zhou, X. Jin, L. Zhang, X. Du, B. Li, A hierarchical nanostructured $Fe_{34}Cr_{34}Ni_{14}Al_{14}Co_4$ high-entropy alloy with good compressive mechanical properties, Mater. Sci. Eng. 716 (2018) 235–239.
[51] R.W. Kozar, A. Suzuki, W.W. Milligan, J.J. Schirra, M.F. Savage, T.M. Pollock, Strengthening mechanisms in polycrystalline multimodal nickel-base superalloys, Metall. Mater. Trans. 40 (7) (2009) 1588–1603.
[52] M.P. Jackson, R.C. Reed, Heat treatment of UDIMET 720Li: the effect of microstructure on properties, Mater. Sci. Eng. 259 (1) (1999) 85–97.
[53] B.K. Zuidema, D.K. Subramanyam, W.C. Leslie, The effect of aluminum on the work hardening and wear resistance of hadfield manganese steel, Metall. Trans. A 18 (9) (1987) 1629–1639.
[54] J.C. Rao, H.Y. Diao, V. Ocelík, D. Vainchtein, C. Zhang, C. Kuo, Z. Tang, W. Guo, J.D. Poplawsky, Y. Zhou, P.K. Liaw, J. Th M. De Hosson, Secondary phases in $Al_xCoCrFeNi$ high-entropy alloys: an in-situ TEM heating study and thermodynamic appraisal ☆, Acta Mater. 131 (2017) 206–220.
[55] X. Yang, Y. Zhang, Prediction of high-entropy stabilized solid-solution in multi-component alloys, Mater. Chem. Phys. 132 (2–3) (2012) 233–238.
[56] Y. Zhang, Y.J. Zhou, J.P. Lin, G.L. Chen, P.K. Liaw, Solid-solution phase formation rules for multi-component alloys, Adv. Eng. Mater. 10 (6) (2008) 534–538.
[57] S. Guo, C. Ng, J. Lu, C.T. Liu, Effect of valence electron concentration on stability of fcc or bcc phase in high entropy alloys, J. Appl. Phys. 109 (10) (2011) 103505.
[58] L.J. Santodonato, Y. Zhang, M. Feygenson, C.M. Parish, M.C. Gao, R.J. Weber, J.C. Neuefeind, Z. Tang, P.K. Liaw, Deviation from high-entropy configurations in the atomic distributions of a multi-principal-element alloy, Nat. Commun. 6 (2015) 5964.
[59] E.A. Marquis, D.N. Seidman, Nanoscale structural evolution of AlSc precipitates in Al(Sc) alloys, Acta Mater. 49 (11) (2001) 1909–1919.
[60] P.W. Voorhees, G.B. Mcfadden, W.C. Johnson, On the morphological development of second-phase particles in elastically-stressed solids, Acta Metall. Mater. 40 (11) (1992) 2979–2992.
[61] D. Tabor, The Hardness of Metals, Oxford University Press[J], New York, 1951.
[62] R.L. Fleischer, Substitutional solution hardening, Acta Metall. 11 (3) (1963) 203–209.
[63] R. Labusch, A statistical theory of solid solution hardening, Phys. Status Solidi 41 (2) (1970) 659–669.
[64] L.A. Gypen, A. Deruyttere, Multi-component solid solution hardening, J. Mater. Sci. 12 (5) (1977) 1034–1038.
[65] I. Toda-Caraballo, E.I. Galindo-Nava, Understanding the factors influencing yield strength on Mg alloys, Acta Mater. 75 (9) (2014) 287–296.
[66] I. Toda-Caraballo, Modelling solid solution hardening in high entropy alloys, Acta Mater. 85 (2015) 14–23.
[67] V.A. Lubarda, On the effective lattice parameter of binary alloys, Mech. Mater. 35 (1) (2003) 53–68.
[68] A.J. Ardell, Precipitation hardening, Metall. Trans. A 16 (12) (1985) 2131–2165.
[69] V. Gerold, H. Haberkorn, On the critical resolved shear stress of solid solutions containing coherent precipitates, Phys. Status Solidi 16 (2) (1966) 675–684.
[70] E. Nembach, Precipitation hardening caused by a difference in shear modulus between particle and matrix, Phys. Status Solidi 78 (2) (1983) 571–581.
[71] T. Hong, A.J. Freeman, Effect of antiphase boundaries on the electronic structure and bonding character of intermetallic systems: NiAl, Phys. Rev. B 43 (8) (1991) 6446.
[72] A.I.H. Committee, J.R. Davis, L.A. Abel, Properties and selection: irons, steels, and high-performance alloys, Metals Handbook 1 (1990).
[73] R.J. Wasilewski, Elastic constants and young's modulus of NiAl, Trans. TMS-AIME 236 (1966) 455–457.
[74] W.F. Hosford, Mechanical Behavior of Materials, Cambridge University Press, New York, America, 2005.
[75] P.B. Hirsch, A. Argon (Ed.), The Physics and Strength of Plasticity, MIT Press, Cambridge, MA, 1969, p. 189.
[76] E. Nembach, Particle Strengthening of Metals and Alloys, Wiley, New York, 1997.
[77] D.N. Seidman, E.A. Marquis, D.C. Dunand, Precipitation strengthening at ambient and elevated temperatures of heat-treatable Al(Sc) alloys, Acta Mater. 50 (16)

(2002) 4021–4035.
[78] Q. Wang, Y. Ma, B. Jiang, X. Li, Y. Shi, C. Dong, P.K. Liaw, A cuboidal B2 nano-precipitation-enhanced body-centered-cubic alloy $Al_{0.7}CoCrFe_2Ni$ with prominent tensile properties, Scripta Mater. 120 (2016) 85–89.
[79] N.J. Petch, The cleavage strength of polycrystals, J Iron Steel Inst 174 (1) (1953) 25–28.
[80] Z. Fu, W. Chen, H. Wen, D. Zhang, Z. Chen, B. Zheng, Y. Zhou, E.J. Lavernia, Microstructure and strengthening mechanisms in an FCC structured single-phase nanocrystalline $Co_{25}Ni_{25}Fe_{25}Al_{7.5}Cu_{17.5}$ high-entropy alloy, Acta Mater. 107 (2016) 59–71.
[81] K.T. Ramesh, Nanomaterials: Mechanics and Mechanisms, Springer, New York, 2009.